

Yin-Yang vortex on UTe₂ (011) surface

Ruotong Yin^{1,#}, Yuanji Li^{1,#}, Zengyi Du^{2,#}, Dengpeng Yuan^{3,#}, Shiyuan Wang¹, Jiashuo Gong¹, Mingzhe Li¹, Ziyuan Chen¹, Jiakang Zhang¹, Yuguang Wang¹, Ziwei Xue³, Xinchun Lai³, Shiyong Tan^{3,*}, Da Wang^{4,5,*}, Qiang-Hua Wang^{4,5,*}, Dong-Lai Feng^{1,6,*}, Ya-Jun Yan^{1,2,*}

¹*Hefei National Research Center for Physical Sciences at the Microscale and Department of Physics, University of Science and Technology of China, Hefei, 230026, China*

²*Hefei National Laboratory, University of Science and Technology of China, Hefei, 230026, China*

³*Science and Technology on Surface Physics and Chemistry Laboratory, Mianyang, 621907, China*

⁴*National Laboratory of Solid State Microstructures and School of Physics, Nanjing University, Nanjing, 210093, China*

⁵*Collaborative Innovation Center of Advanced Microstructures, Nanjing University, Nanjing, 210093, China*

⁶*National Synchrotron Radiation Laboratory, School of Nuclear Science and Technology, and New Cornerstone Science Laboratory, University of Science and Technology of China, Hefei, 230026, China*

Those authors contributed equally to this work.

*E-mails: sytan4444@163.com, dawang@nju.edu.cn, qhwang@nju.edu.cn, dlffeng@ustc.edu.cn, yanyj87@ustc.edu.cn;

UTe₂ is a promising candidate for spin-triplet superconductor, yet its exact superconducting order parameter remains highly debated. Here, via scanning tunneling microscopy/spectroscopy, we observe a novel type of magnetic vortex with distinct dark-bright contrast in the local density of states on the UTe₂ (011) surface under a perpendicular magnetic field, resembling the Yin-Yang diagram in Taoism. Each Yin-Yang vortex contains a quantized magnetic flux, and the boundary between the Yin and Yang parts aligns with the crystallographic *a*-axis of UTe₂. The vortex states exhibit intriguing behaviors — a sharp zero-energy conductance peak exists at the Yang part, while a superconducting gap feature with pronounced coherence peaks exists at the Yin part, which is even sharper than those measured far from the vortex core or in the absence of magnetic field. Assisted by numerical simulations, we show that the Yin-Yang vortices on the UTe₂ (011) surface arise from the interplay between the gapless surface states associated with spin-triplet pairing and the vortex bound states because of the cylindrical squarish Fermi surface of UTe₂. Therefore, the observation of Yin-Yang vortex is strong evidence of the gapless surface states on UTe₂ (011) surface, which rules out the possibility of B_{2u} pairing symmetry.

Since the discovery of superfluidity in ³He five decades ago, physicists have been fascinated by the prospect of its spin-triplet superconducting analogs¹⁻³. UBe₁₃ and UPt₃ are likely candidates with many unconventional superconducting properties^{4,5}, but their low superconducting critical temperature (T_c) limits extensive experimental studies. Since 2019, UTe₂ has emerged as a new promising candidate for spin-triplet superconductors, the relatively high T_c and recently improved sample quality have enabled the acquisition of further evidence supporting its triplet pairing nature⁶⁻³⁹, including the large and highly anisotropic upper critical field exceeding the Pauli limit^{6,7}, weak temperature dependence of the Knight shift across the superconducting transition^{9,22,32,38}, multiple

reentrant superconducting phases under high magnetic fields^{8,11,13,18}, chiral in-gap states at step edges of UTe₂ (011) surface by low-temperature scanning tunneling microscopy measurements¹⁷, etc.

UTe₂ crystallizes in a body-centered orthorhombic structure with D_{2h} point group symmetry. In the presence of strong spin-orbit coupling, four distinct single-component spin-triplet superconducting order parameters are allowed: A_u , B_{1u} , B_{2u} , and B_{3u} (Ref. 23). Among them, A_u generally corresponds to a fully gapped superconducting state, while gap nodes exist for B_{1u} , B_{2u} , and B_{3u} states along the crystalline c -, b -, and a -axes, respectively. Moreover, it is possible for multicomponent superconductivity arising from linear combinations of these four order parameters, which breaks time reversal symmetry (TRS)⁴⁰. Experimentally, evidence of TRS breaking was observed in UTe₂ with $T_c \sim 1.6$ K (Refs. 24, 26), but the latest results of Kerr and muon spin relaxation (μ SR) measurements on high-quality UTe₂ with $T_c \sim 2$ K deny it^{41,42}. Thus, the superconducting state in UTe₂ is most likely time-reversal invariant and possesses a single component, but exactly which form remains controversial. Furthermore, thermal conductivity^{14,43}, specific heat^{19,33} and penetration depth⁴⁴ measurements demonstrate the presence of nodal quasiparticles in the superconducting state of UTe₂, favoring B_{1u} , B_{2u} , and B_{3u} over fully gapped A_u state. More order-parameter sensitive experiments are needed to distinguish these three pairing symmetries.

The behaviors of magnetic vortex can provide critical clues on the nature of the superconducting order parameters. For instance, in an anisotropic or nodal superconductor, vortex structures may exhibit complex spatial patterns or nodal features⁴⁵⁻⁴⁸; In topological superconductors, Majorana zero modes are expected to emerge at the vortex core⁴⁹⁻⁵². However, due to the previously limited sample quality, direct imaging of magnetic vortex and study of vortex states in UTe₂ remains elusive. Here, we use scanning tunneling microscopy/spectroscopy (STM/STS) with ultralow-temperature and high-magnetic-field capabilities to investigate the magnetic vortex properties on the (011) surface of high-quality UTe₂ crystals. We directly observe a novel type of vortex featuring a Yin-Yang-like spatial contrast, and combined with numerical simulations, we attribute its appearance to the interplay between the gapless surface states associated with spin-triplet superconductivity and the vortex bound state because of the cylindrical squarish Fermi surface of UTe₂.

The crystal structure of UTe₂ is shown in Fig. 1a, where the commonly reported easy-cleave plane, the (011) plane, is indicated by the yellow plane. The (011) plane consists of chains of Te1, Te2 and U atoms aligned along the crystallographic a -axis, with their atomic heights arranged in descending order [Fig. 1b]. The UTe₂ crystals used in this study are synthesized via the molten salt flux method, which show a $T_{c,0}$ of ~ 2 K and residual resistance ratio of ~ 82 (Supplementary note 1). Figure 1c shows the typical topographic image of the exposed surface of UTe₂ after cleavage, exhibiting chain-like structures along the a -axis; A higher-resolution image [Fig. 1d] resolves two alternating atomic chains with different heights, which are assigned as Te1 and Te2, respectively. The measured interatomic spacing along the Te1 chain and the interchain spacing between adjacent Te1 chains are $a = 4.05$ Å and $b^* = 7.6$ Å, consistent with the lattice parameters of UTe₂ (011) plane (Refs. 6, 53), as well as the previously reported STM results on UTe₂ (011) surface^{17,39,54-57}. Here we define the perpendicular direction to a -axis on UTe₂ (011) surface as the b^* -axis to distinguish from the crystallographic b -axis.

Figure 1e,f show the spatial evolution of superconducting gap spectra along the Te2 chain (cut

#1) and perpendicular to it (cut #2). The superconducting gap is obvious and homogeneous along the Te2 chain, with a gap size of ~ 0.25 meV judging from the coherence peak positions and an averaged gap depth of $\sim 15\%$ defined by $1 - g(0 \text{ meV})/g(1 \text{ meV})$, with $g(E)$ representing the dI/dV value at the energy of E . By contrast, the superconducting gap varies significantly along the b^* -axis, which is consistent with previous reports¹⁷. It is noteworthy that the observed shallow superconducting gap reflects the intrinsic property of UTe_2 , as the superconducting gap of Al polycrystal with $T_c \sim 1.2$ K measured under the same conditions is sharp, showing 100% gap depth (Supplementary note 2). Taking account of existing studies^{14,19,24,32,33,43,44,58}, this might be explained by considering that UTe_2 is a spin-triplet superconductor with intrinsic gap nodes and gapless surface states, which contribute to the residual zero-energy density of states (DOS).

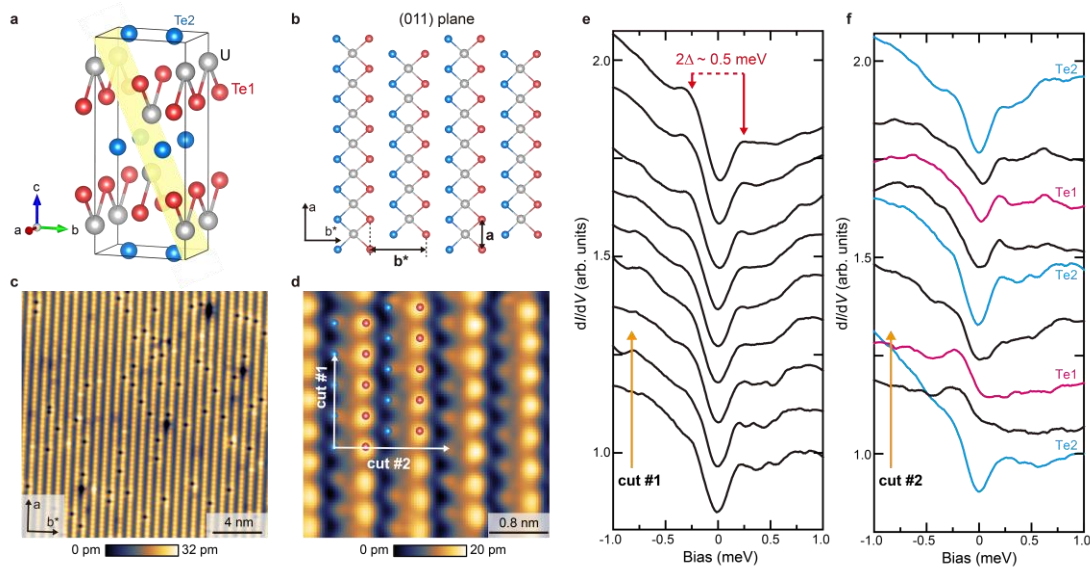


Fig. 1 | Crystal structure and superconducting gap spectra of UTe_2 . **a**, Crystal structure of UTe_2 . The easy-cleave plane is the (011) plane as indicated by the yellow shaded plane. **b**, Projected atomic structure of the (011) plane. **c**, Typical topographic image of the exposed (011) surface of UTe_2 . **d**, Zoomed-in view of the atomic lattice with higher resolution, with the schematic Te1 and Te2 atoms overlaid on top. **e,f**, dI/dV spectra taken along trajectories of cuts #1 and #2 as indicated in panel (d). Measurement conditions: (c) $V_b = 200$ mV, $I_t = 50$ pA; (d) $V_b = 100$ mV, $I_t = 100$ pA; (e,f) $V_b = 1$ mV, $I_t = 100$ pA, $\Delta V = 50$ μ V.

Subsequently, we measure the magnetic vortex properties on UTe_2 (011) surface. Figure 2a shows the topographic image of a selected sample region of $190 \times 190 \text{ nm}^2$, and the raw vortex maps, $g(\mathbf{r}, E) = dI/dV(\mathbf{r}, E)$, collected in this field of view under different perpendicular magnetic fields (\mathbf{B}_\perp) are displayed in Supplementary Fig. 3, where unique vortex patterns can be resolved. To enhance contrast, we defined normalized vortex maps $C(\mathbf{r}, 0.25 \text{ meV}) = g(\mathbf{r}, 0 \text{ meV})/g(\mathbf{r}, 0.25 \text{ meV})$, that is dividing the raw vortex map at zero-energy by that at coherence peak energy, which are presented in Fig. 2b-g. In the absence of magnetic field, the local DOS (LDOS) distribution exhibits some spatial inhomogeneity but no discernible patterns can be resolved [Fig. 2b]. Under $\mathbf{B}_\perp = 0.25$ T, bright stripes appear along the a -axis as indicated by the blue arrow in Fig. 2c, accompanied by a peculiar dark core with suppressed LDOS on its right side (white arrow). Such vortex pattern with paired bright-dark cores is intrinsic to the UTe_2 (011) surface, which remains unchanged when the STM scanning direction is changed or the direction of \mathbf{B}_\perp is

reversed, as discussed in Supplementary note 4. Moreover, it persists to higher B_{\perp} values [Fig. 2d-g], with its number increasing proportionally with increasing B_{\perp} , and finally becomes invisible at $B_{\perp} > 8$ T (Supplementary Fig. 3). Figure 2h summarizes the number of the paired bright-dark cores as a function of B_{\perp} , which fits well with the theoretical value of $n = \frac{B_{\perp} S}{\Phi_0}$, with S and Φ_0 are the scan area and the magnetic flux quantum, demonstrating that each paired bright-dark cores contains a quantized magnetic flux. To our knowledge, there is no prior report of such kind of magnetic vortex, which we term "Yin-Yang" vortex in this study, as its dark-bright parts conjugate like the Yin-Yang diagram.

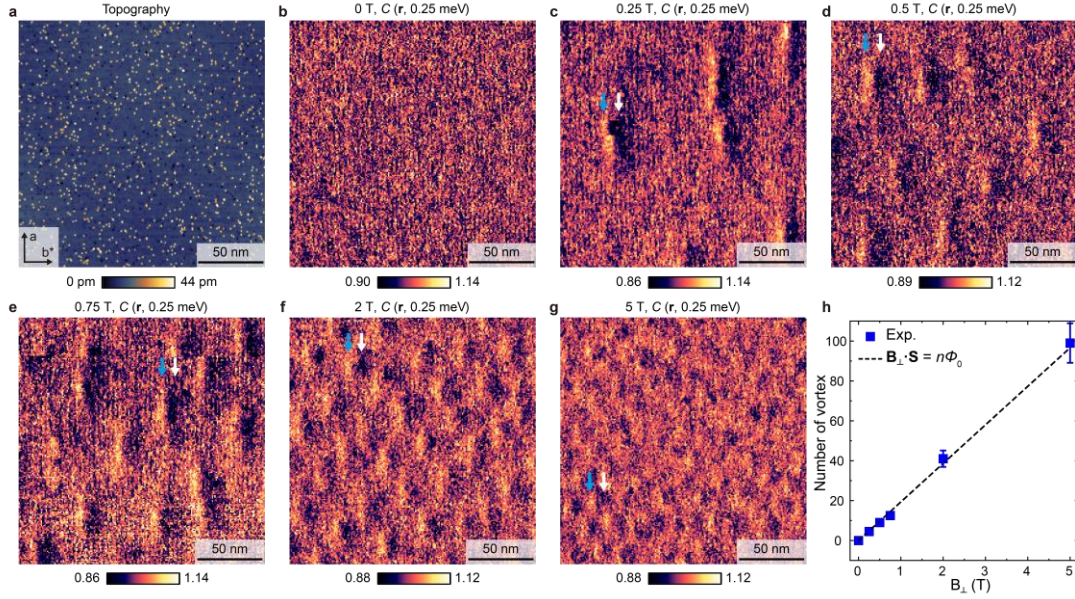


Fig. 2 | Vortex maps on UTe₂ (011) surface under varying B_{\perp} . **a**, Topographic image of the selected sample region for vortex mapping. **b-g**, Normalized vortex maps under various B_{\perp} . **h**, Evolution of vortex number as a function of B_{\perp} , with theoretical values shown by the dashed line. Measurement conditions: **(a)** $V_b = 100$ mV, $I_t = 30$ pA; **(b,d,f,g)** $V_b = -1.5$ mV, $I_t = 80$ pA, $\Delta V = 100$ μ V; **(c,e)** $V_b = -1.5$ mV, $I_t = 400$ pA, $\Delta V = 80$ μ V.

Figure 3a shows the detailed distribution of a single Yin-Yang vortex measured at $B_{\perp} = 0.5$ T, the LDOS contrast between the Yang and Yin parts of the vortex is clearly resolved. Typical dI/dV spectra measured at the Yang part (point A in Fig. 3a with higher zero-energy DOS), Yin part (point B in Fig. 3a with lower zero-energy DOS) of the vortex, locations away from the vortex, and that under zero magnetic field are plotted together in Fig. 3b for comparison. Far away from the vortex core, a shallow gap with subtle coherence peaks is observed, resembling that observed in the absence of magnetic field, which is probably induced by the inherent nodal gap structure and gapless surface states of spin-triplet superconductivity in UTe₂ as discussed above. In the vortex core, the dI/dV spectrum at the Yang part exhibits a sharp zero-energy conductance peak (ZEC) with a full width at half maximum (FWHM) of ~ 0.2 meV, persisting to tens of nanometers along the a -axis without obvious splitting (Supplementary note 5), which may result from the superposition of Caroli-de-Gennes-Matignon (CdGM) bound states and gapless surface states; whereas in strong contrast, the dI/dV spectrum at the Yin part shows a superconducting gap with pronounced coherence peaks that are even sharper than those measured far from the vortex core or under zero magnetic field, which

is puzzling and suggests reduced contribution of the CdGM states and the gapless surface states near Fermi level.

Figure 3c,d display typical line profiles of the vortex acquired along cuts #3 and #4 in Fig. 3a, respectively. In Fig. 3c, a single-exponential function was used to fit the data and extract the Ginzburg-Landau coherence length along a -axis, the obtained results for multiple vortices are shown in Fig. 3e, yielding an averaged $\xi_a = 15.1 \pm 4.8$ nm. In Fig. 3d, a double-exponential fitting model was applied to separately extract the coherence lengths of the vortex's Yang and Yin parts (ξ_{Yang} and ξ_{Yin}) along b^* -axis, as well as the center-to-center distance between them, $d_{\text{Yin-Yang}}$. The corresponding results for multiple vortices, along with the values of $\xi_{\text{Yang}} + \xi_{\text{Yin}}$, are presented in Fig. 3f,g, and the averaged values of ξ_{Yang} , ξ_{Yin} , $\xi_{\text{Yang}} + \xi_{\text{Yin}}$, and $d_{\text{Yin-Yang}}$ are approximately 4.5 ± 1.4 nm, 7.5 ± 2.1 nm, 12.0 ± 2.7 nm, and 10.6 ± 2.7 nm, respectively (see Supplementary note 6 for more fitting details). Two notable features emerge: (i) ξ_{Yang} is significantly smaller than ξ_{Yin} , and intriguingly, (ii) $d_{\text{Yin-Yang}}$ approximates the sum $\xi_{\text{Yang}} + \xi_{\text{Yin}}$. Taking $\xi_{\text{Yang}} + \xi_{\text{Yin}}$ as the coherence length along b^* -axis, ξ_{b^*} , the resulting ratio of $\xi_a:\xi_{b^*}$ is ~ 1.3 , which is likely due to the anisotropy of Fermi surface and superconducting gap structure.

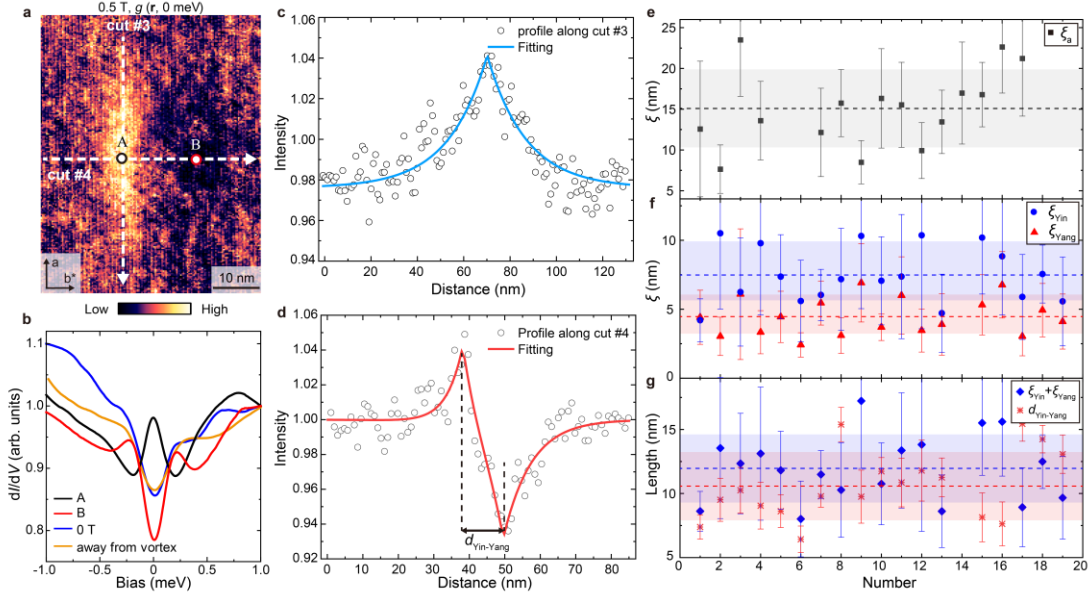


Fig. 3 | Detailed properties of the Yin-Yang vortex. **a**, Detailed distribution of a single Yin-Yang vortex. **b**, Typical dI/dV spectra collected at the Yin and Yang parts of the vortex, as marked out by the red and black dots in panel (a). The spectra measured at the locations away from the vortex and under zero magnetic field are listed as well for comparison. **c,d**, Exponential fits to the line profiles of the vortex, taken along the trajectories of cuts #3 and #4 as indicated in panel (a). **e-g**, Statistics of the fitted Ginzburg-Landau coherence lengths along the two lattice directions and $d_{\text{Yin-Yang}}$ for vortices measured under $B_{\perp} = 0.25\text{-}0.75$ T. Measurement conditions: **(a)** $V_b = -1.5$ mV, $I_t = 400$ pA, $\Delta V = 80$ μ V; **(b)** $V_b = 1$ mV, $I_t = 100\text{-}400$ pA, $\Delta V = 50$ μ V.

To unravel the formation mechanism of Yin-Yang vortex on UTe_2 (011) surface, we performed numerical simulations, and the results are displayed in Fig. 4, and more details are discussed in Supplementary note 7. To mimic the square-shaped cylindrical Fermi surfaces of UTe_2 as previously proposed by the theoretical and experimental studies^{12,16,35,59-63}, we construct a single-orbital tight-binding model on the cubic lattice, to obtain a cylindrical squarish Fermi surface as shown in Fig.

4a. Then we solve the Bogoliubov-de Gennes (BdG) Hamiltonian in presence of a single vortex for the four types of spin-triplet pairing symmetries on the tilted lattice with (011) surface. The typical simulation results of the zero-energy LDOS, with the same value for all symmetry-allowed \mathbf{d} -vectors, are plotted in Fig. 4b-e. All of A_u , B_{1u} and B_{3u} pairings can give the Yin-Yang vortex pattern. Moreover, the Yin part of the vortex appears more extended than the Yang part, qualitatively consistent with our experimental observations (Fig. 3a,f).

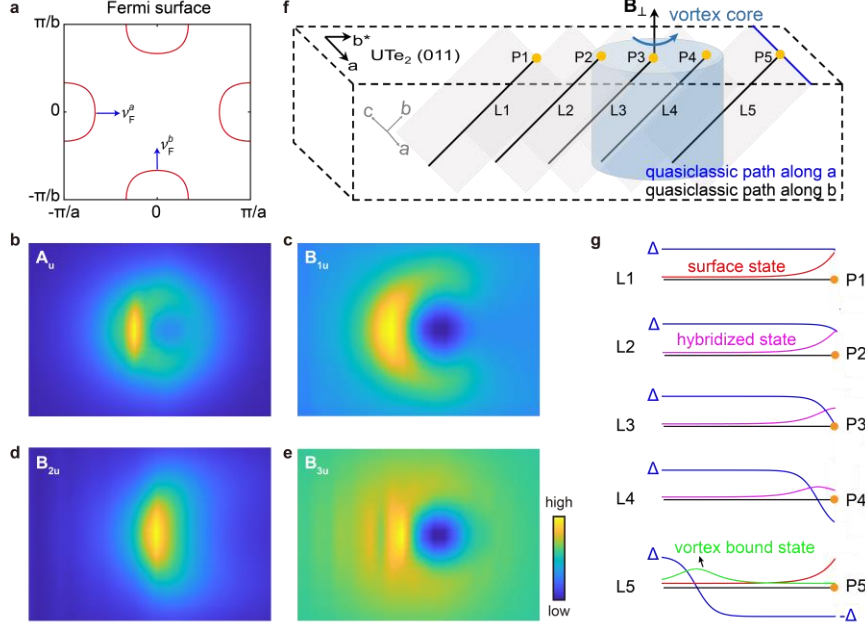


Fig. 4 | Numerical results of zero-energy LDOS on UTe₂ (011) surface for the four types of spin-triplet pairing symmetries. **a**, Squarish Fermi surface used for numerical simulations, with the Fermi velocity along \mathbf{a} - and \mathbf{b} -axes marked out by the blue arrows. **b-e**, Numerical results of zero-energy LDOS on UTe₂ (011) surface for the four types of spin-triplet pairing symmetries, the vortex center is at the middle in each plot. **f**, Sketch of the typical classical paths with Fermi velocity \mathbf{v}_F along \mathbf{b} -axis (black lines L1 to L5) and along \mathbf{a} -axis (blue line). The end points of paths L1-L5 on the (011) surface are labeled as P1-P5, respectively. **g**, Sketch of pairing function Δ (blue curve) along paths L1-L5, respectively. The zero-energy surface state (red curve), vortex bound state (green curve) and their hybridized state (magenta curve) are schematically plotted as well for each path.

The above numerical results can be understood in a quasi-classical picture. Assuming k_F^{-1} is much smaller than the superconducting coherence length ξ , i.e. satisfying the quasi-classical condition, the LDOS $\rho(\omega, \mathbf{r})$ (proportional to the dI/dV value in STM) is contributed by summing the classical paths along different Fermi velocities \mathbf{v}_F on the Fermi surface, i.e. $\rho(\omega, \mathbf{r}) = \int_{k_F} \rho_{k_F}(\omega, \mathbf{r})$. For the square-shaped Fermi surface in UTe₂, there are mainly two classical paths, along crystallographic \mathbf{a} - and \mathbf{b} -axes as indicated by arrows in Fig. 4a, to pass through each position \mathbf{r} . This brings great simplification for our analysis to explain the observed Yin-Yang vortex bound states on UTe₂ (011) surface. Let us consider five typical paths L1 to L5 along \mathbf{b} -axis with $\mathbf{k}_F \parallel \mathbf{b}$ for simplicity [Fig. 4f]. For A_u , B_{1u} and B_{3u} , each path can be mapped to a one-dimensional p -wave superconductor, and thus always possesses at least one zero-energy mode, as depicted in Fig. 4g. For L1, the zero-energy mode is the topologically protected surface state. For L5, there are two zero-

energy modes, one at the boundary as the surface mode similar to L1, and the other near the vortex center as the vortex bound state. For L2 to L4, the surface state and the vortex bound state hybridize and only one zero-energy mode is left. The wave function of the zero-energy mode becomes more and more extensive from L2 to L4. As a result, the amplitude of the wave function at the boundary (contributing to zero-energy LDOS in STM) drops from P2 to P4, which suppresses the LDOS asymmetrically (P4 deeper than P2). On the other hand, for the paths along a -axis, there are no contributions from surface states (which, if exist, reside at the ends of these paths) and only vortex bound states near the vortex, which enhance the LDOS symmetrically (P4 equal to P2). Combining the above two effects together, we acquire a basic understanding of the Yin-Yang pattern of the vortex bound states on UTe₂ (011) surface.

Based on the above quasi-classical picture, we understand that the Yin-Yang vortex pattern is caused by the interplay between the gapless surface states and the vortex bound state because of the cylindrical squarish Fermi surface of UTe₂. Therefore, it is strong evidence for the existence of the gapless surface state on the UTe₂ (011) surface, which requires a k_b -component in the \mathbf{d} -vector, hence, the B_{2u} pairing can be safely excluded in general, but the remaining three candidates of A_u , B_{1u} and B_{3u} cannot be identified exclusively only by this Yin-Yang vortex feature. Given that the presence of nodal quasiparticles in the superconducting state of UTe₂ is extensively demonstrated by thermal conductivity^{14,43}, specific heat^{19,33}, penetration depth⁴⁴ and STM measurements^{17,39,55}, we are left with A_u with accidental nodes, or B_{1u} and B_{3u} in general. The locations of the nodes are closely related to the order parameter symmetry and the Fermi surface topology. Based on most available reports for the band structure of UTe₂^{35,59-63}, two square-shaped cylindrical Fermi surfaces exist around $(\pm \frac{\pi}{a}, 0)$ and $(0, \pm \frac{\pi}{b})$, and in this case, the B_{1u} symmetry can be excluded since its nodes exist at $k_a = 0, \pm \frac{\pi}{a}, k_b = 0, \pm \frac{\pi}{b}$. However, there is also experiments reporting the existence of a small 3D Fermi surface around $(0, 0, \frac{\pi}{c})$ (Refs. 16,64), which allows the presence of nodes for B_{1u} symmetry. Further determination of the exact Fermi surface topology of UTe₂ is urgent to clarify this point.

Notes: During the preparation of this manuscript, we noticed another two works by Yang et al.⁶⁵ and Sharma et al.⁶⁶ reporting similar magnetic vortex structure and vortex states in UTe₂ (011) surface by STM measurements.

Methods

Synthesis of UTe₂ single crystals. High-quality UTe₂ single crystals were synthesized via the molten salt flux (MSF) technique employing an equimolar NaCl-KCl mixture (99.99% purity, Alfa Aesar) as a flux. Uranium metal pieces (mass < 0.4 g) were initially etched in nitric acid to eliminate surface oxides. Under an argon atmosphere in a glovebox, tellurium pieces (Te, 99.999% purity, Alfa Aesar) were combined with uranium at a U:Te molar ratio of 1:1.65, along with NaCl-KCl flux at a U:salt molar ratio of 1:60. The reactants were loaded into a carbon crucible lined with quartz wool to prevent material loss during heating. Then the crucible was placed in a quartz tube and heated to 180 °C under high vacuum ($< 5 \times 10^{-4}$ Pa) for dehydration. Subsequently, the ampoule was vacuum-sealed and placed in a box furnace, where the mixture was heated to 950 °C over 24 hours

and maintained at this temperature for 48 hours. It was then cooled gradually at a rate of 0.03 °C/min to 650 °C, held at this temperature for 48 hours, and finally cooled to ambient temperature naturally. After the growth process, the ampoules and crucibles were mechanically cleaved, and bulk UTe₂ crystals were manually collected and stored under an argon atmosphere to prevent oxidation.

Sample characterizations. Temperature dependent resistivity measurements were conducted in a Quantum Design DynaCool Physical Properties Measurement System (PPMS-9T), by using a standard four-probe configuration.

STM measurements. UTe₂ crystals were mechanically cleaved at 80 K in ultrahigh vacuum with a base pressure better than 2×10^{-10} mbar and immediately transferred into a UNISOKU-1600 STM. Pt-Ir tips were used for STM measurements after being treated on a clean Au (111) substrate. The dI/dV spectra were collected by a standard lock-in technique with a modulation frequency of 973 Hz and a modulation amplitude ΔV of 50-100 μ V. The data in the main text were collected at ~ 40 mK with an effective electron temperature T_{eff} of ~ 170 mK.

Acknowledgments

We thank Prof. Ziqiang Wang for helpful discussions. This work is supported by National Key R&D Program of the MOST of China (Grants No. 2023YFA1406304 (Y.J.Y.), No. 2022YFA1403201 (D.W.)), the National Natural Science Foundation of China (Grants No. 12374140 (Y.J.Y.), No. 12374147 (Q.H.W.), No. 12274205 (D.W.), No. 92365203 (Q.H.W.), No. U23A20580 (S.Y.T.), No. 12494593 (Y.J.Y.)), the Innovation Program for Quantum Science and Technology (Grant No. 2021ZD0302803 (D.L.F.)), the New Cornerstone Science Foundation (D.L.F.), Sichuan Science and Technology Program (2025NSFJQ0040 (S.Y.T.)).

Author contributions

UTe₂ single crystals were grown by D. Y., S. T. and X. L.; STM measurements were performed by R. Y. and Y. L.; Data analysis was performed by R. Y., Y. L., S. W., J. G., M. L., Z. C., J. Z., Y. W., Z. D. and Y. Y.; numerical simulation was done by D. W. and Q. W.; Z. D., D. W., Y. Y. and D. F. coordinated the whole work and wrote the manuscript. All authors have discussed the results and the interpretation.

Competing interests

The authors declare no competing interests.

References

1. Leggett, A. J. A theoretical description of the new phases of liquid ³He. *Rev. Mod. Phys.* **47**, 331 (1975).
2. Mizushima, T., Tsutsumi, Y., Kawakami, T., Sato, M., Ichioka, M. & Machida, K. Symmetry-Protected Topological Superfluids and Superconductors —From the Basics to ³He—. *J. Phys. Soc. Jpn.* **85**, 022001 (2016).
3. Sato, M. & Ando, Y. Topological superconductors: a review. *Rep. Prog. Phys.* **80**, 076501 (2017).
4. Ott, H. R., Rudigier, H., Fisk, Z. & Smith, J. L. UBe₁₃: An Unconventional Actinide Superconductor. *Phys. Rev. Lett.* **50**, 1595 (1983).

5. Joynt, R. & Taillefer, L. The superconducting phases of UPt_3 . *Rev. Mod. Phys.* **74**, 235 (2002).
6. Ran, S., *et al.* Nearly ferromagnetic spin-triplet superconductivity. *Science* **365**, 684 (2019).
7. Aoki, D., *et al.* Unconventional Superconductivity in Heavy Fermion UTe_2 . *J. Phys. Soc. Jpn.* **88**, 043702 (2019).
8. Knebel, G., *et al.* Field-Reentrant Superconductivity Close to a Metamagnetic Transition in the Heavy-Fermion Superconductor UTe_2 . *J. Phys. Soc. Jpn.* **88**, 063707 (2019).
9. Tokunaga, Y., *et al.* ^{125}Te -NMR Study on a Single Crystal of Heavy Fermion Superconductor UTe_2 . *J. Phys. Soc. Jpn.* **88**, 073701 (2019).
10. Sundar, S., *et al.* Coexistence of ferromagnetic fluctuations and superconductivity in the actinide superconductor UTe_2 . *Phys. Rev. B* **100**, 140502(R) (2019).
11. Braithwaite, D., *et al.* Multiple superconducting phases in a nearly ferromagnetic system. *Commun. Phys.* **2**, 147 (2019).
12. Ishizuka, J., Sumita, S., Daido, A. & Yanase, Y. Insulator-Metal Transition and Topological Superconductivity in UTe_2 from a First-Principles Calculation. *Phys. Rev. Lett.* **123**, 217001 (2019).
13. Ran, S., *et al.* Extreme magnetic field-boosted superconductivity. *Nat. Phys.* **15**, 1250 (2019).
14. Metz, T., *et al.* Point-node gap structure of the spin-triplet superconductor UTe_2 . *Phys. Rev. B* **100**, 220504(R) (2019).
15. Nevidomskyy, A. H. Stability of a nonunitary triplet pairing on the border of magnetism in UTe_2 . arXiv: 2001.02699 (2020).
16. Miao, L., *et al.* Low Energy Band Structure and Symmetries of UTe_2 from Angle-Resolved Photoemission Spectroscopy. *Phys. Rev. Lett.* **124**, 076401 (2020).
17. Jiao, L., *et al.* Chiral superconductivity in heavy-fermion metal UTe_2 . *Nature* **579**, 523 (2020).
18. Aoki, D., *et al.* Multiple Superconducting Phases and Unusual Enhancement of the Upper Critical Field in UTe_2 . *J. Phys. Soc. Jpn.* **89**, 053705 (2020).
19. Kittaka, S., *et al.* Orientation of point nodes and nonunitary triplet pairing tuned by the easy-axis magnetization in UTe_2 . *Phys. Rev. Res.* **2**, 032014(R) (2020).
20. Thomas, S. M., *et al.* Evidence for a pressure-induced antiferromagnetic quantum critical point in intermediate-valence UTe_2 . *Sci. Adv.* **6**, eabc8709 (2020).
21. Duan, C., *et al.* Incommensurate Spin Fluctuations in the Spin-Triplet Superconductor Candidate UTe_2 . *Phys. Rev. Lett.* **125**, 237003 (2020).
22. Nakamine, G., *et al.* Anisotropic response of spin susceptibility in the superconducting state of UTe_2 probed with ^{125}Te -NMR measurement. *Phys. Rev. B* **103**, L100503 (2021).
23. Shishidou, T., Suh, H. G., Brydon, P. M. R., Weinert, M. & Agterberg, D. F. Topological band and superconductivity in UTe_2 . *Phys. Rev. B* **103**, 104504 (2021).
24. Bae, S., *et al.* Anomalous normal fluid response in a chiral superconductor UTe_2 . *Nat. Commun.* **12**, 2644 (2021).
25. Ishizuka, J. & Yanase, Y. Periodic Anderson model for magnetism and superconductivity in UTe_2 . *Phys. Rev. B* **103**, 094504 (2021).
26. Hayes, I. M., *et al.* Multicomponent superconducting order parameter in UTe_2 . *Science* **373**, 797 (2021).
27. Knafo, W., *et al.* Low-dimensional antiferromagnetic fluctuations in the heavy-fermion paramagnetic ladder compound UTe_2 . *Phys. Rev. B* **104**, L100409 (2021).
28. Willa, K., *et al.* Thermodynamic signatures of short-range magnetic correlations in UTe_2 . *Phys.*

- Rev. B* **104**, 205107 (2021).
29. Thomas, S. M., *et al.* Spatially inhomogeneous superconductivity in UTe_2 . *Phys. Rev. B* **104**, 224501 (2021).
 30. Duan, C., *et al.* Resonance from antiferromagnetic spin fluctuations for superconductivity in UTe_2 . *Nature* **600**, 636 (2021).
 31. Haga, Y., *et al.* Effect of uranium deficiency on normal and superconducting properties in unconventional superconductor UTe_2 . *J. Phys.: Condens. Matter* **34**, 175601 (2022).
 32. Fujibayashi, H., *et al.* Superconducting Order Parameter in UTe_2 Determined by Knight Shift Measurement. *J. Phys. Soc. Jpn.* **91**, 043705 (2022).
 33. Rosa, P. F. S., *et al.* Single thermodynamic transition at 2 K in superconducting UTe_2 single crystals. *Commun. Mater.* **3**, 33 (2022).
 34. Sakai, H., *et al.* Single crystal growth of superconducting UTe_2 by molten salt flux method. *Phys. Rev. Mater.* **6**, 073401 (2022).
 35. Aoki, D., *et al.* First Observation of the de Haas–van Alphen Effect and Fermi Surfaces in the Unconventional Superconductor UTe_2 . *J. Phys. Soc. Jpn.* **91**, 083704 (2022).
 36. Eo, Y. S., *et al.* c-axis transport in UTe_2 : Evidence of three-dimensional conductivity component. *Phys. Rev. B* **106**, L060505 (2022).
 37. Ishihara, K., *et al.* Anisotropic enhancement of lower critical field in ultraclean crystals of spin-triplet superconductor candidate UTe_2 . *Phys. Rev. Res.* **5**, L022002 (2023).
 38. Matsumura, H., *et al.* Large Reduction in the *a*-axis Knight Shift on UTe_2 with $T_c = 2.1$ K. *J. Phys. Soc. Jpn.* **92**, 063701 (2023).
 39. Gu, Q., *et al.* Pair Wavefunction Symmetry in UTe_2 from Zero-Energy Surface State Visualization. arXiv: 2501. 16636 (2025).
 40. Shaffer, D. & Chichinadze, D. V. Chiral superconductivity in UTe_2 via emergent C_4 symmetry and spin-orbit coupling. *Phys. Rev. B* **106**, 014502 (2022).
 41. Ajeesh, M. O., *et al.* Fate of Time-Reversal Symmetry Breaking in UTe_2 . *Phys. Rev. X* **13**, 041019 (2023).
 42. Azari, N., *et al.* Absence of Spontaneous Magnetic Fields due to Time-Reversal Symmetry Breaking in Bulk Superconducting UTe_2 . *Phys. Rev. Lett.* **131**, 226504 (2023).
 43. Hayes, I. M., *et al.* Robust nodal behavior in the thermal conductivity of superconducting UTe_2 . arXiv: 2402.19353 (2024).
 44. Ishihara, K., *et al.* Chiral superconductivity in UTe_2 probed by anisotropic low-energy excitations. *Nat. Commun.* **14**, 2966 (2023).
 45. Song, C.-L., *et al.* Direct Observation of Nodes and Twofold Symmetry in FeSe Superconductor. *Science* **332**, 1410 (2011).
 46. Hanaguri, T., Kitagawa, K., Matsubayashi, K., Mazaki, Y., Uwatoko, Y. & Takagi, H. Scanning tunneling microscopy/spectroscopy of vortices in LiFeAs . *Phys. Rev. B* **85**, 214505 (2012).
 47. Fan, Q., *et al.* Scanning tunneling microscopy study of superconductivity, magnetic vortices, and possible charge-density wave in $\text{Ta}_4\text{Pd}_3\text{Te}_{16}$. *Phys. Rev. B* **91**, 104506 (2015).
 48. Tao, R., *et al.* Direct Visualization of the Nematic Superconductivity in $\text{Cu}_x\text{Bi}_2\text{Se}_3$. *Phys. Rev. X* **8**, 041024 (2018).
 49. Liu, Q., *et al.* Robust and Clean Majorana Zero Mode in the Vortex Core of High-Temperature Superconductor $(\text{Li}_{0.84}\text{Fe}_{0.16})\text{OHFeSe}$. *Phys. Rev. X* **8**, 041056 (2018).
 50. Yuan, Y., *et al.* Evidence of anisotropic Majorana bound states in 2M- WS_2 . *Nat. Phys.* **15**, 1046

(2019).

51. Li, M., *et al.* Ordered and tunable Majorana-zero-mode lattice in naturally strained LiFeAs. *Nature* **606**, 890 (2022).
52. Wang, D., *et al.* Evidence for Majorana bound states in an iron-based superconductor. *Science* **362**, 333 (2018).
53. Haneveld, A. J. K. & Jellinek, F. The crystal structure of stoichiometric uranium ditelluride. *J. Less Common Met.* **21**, 45 (1970).
54. Aishwarya, A., *et al.* Magnetic-field-sensitive charge density waves in the superconductor UTe₂. *Nature* **618**, 928 (2023).
55. Gu, Q., *et al.* Detection of a pair density wave state in UTe₂. *Nature* **618**, 921 (2023).
56. LaFleur, A., *et al.* Inhomogeneous high temperature melting and decoupling of charge density waves in spin-triplet superconductor UTe₂. *Nat. Commun.* **15**, 4456 (2024).
57. Aishwarya, A., *et al.* Melting of the charge density wave by generation of pairs of topological defects in UTe₂. *Nat. Phys.* **20**, 964 (2024).
58. Li, Z., *et al.* Observation of odd-parity superconductivity in UTe₂. arXiv: 2309.08668 (2023).
59. Choi, H. C., Lee, S. H. & Yang, B.-J. Correlated normal state fermiology and topological superconductivity in UTe₂. *Commun. Phys.* **7**, 273 (2024).
60. Xu, Y., Sheng, Y. & Yang, Y. F. Quasi-Two-Dimensional Fermi Surfaces and Unitary Spin-Triplet Pairing in the Heavy Fermion Superconductor UTe₂. *Phys. Rev. Lett.* **123**, 217002 (2019).
61. Aoki, D., Sheikin, I., Marquardt, N., Lapertot, G., Flouquet, J. & Knebel, G. High Field Superconducting Phases of Ultra Clean Single Crystal UTe₂. *J. Phys. Soc. Jpn.* **93**, 123702 (2024).
62. Weinberger, T. I., *et al.* Quantum Interference between Quasi-2D Fermi Surface Sheets in UTe₂. *Phys. Rev. Lett.* **132**, 266503 (2024).
63. Eaton, A. G., *et al.* Quasi-2D Fermi surface in the anomalous superconductor UTe₂. *Nat. Commun.* **15**, 223 (2024).
64. Fujimori, S.-i., *et al.* Electronic Structure of UTe₂ Studied by Photoelectron Spectroscopy. *J. Phys. Soc. Jpn.* **88**, 103701 (2019).
65. Yang, Z., *et al.* Magnetization-induced symmetry breaking in the superconducting vortices of UTe₂. arXiv: 2503.13143 (2025).
66. Sharma, N., *et al.* Observation of Persistent Zero Modes and Superconducting Vortex Doublets in UTe₂. arXiv: 2503.17450 (2025).